

#1 - Ultrasound-bioluminescence hybrid modality imaging in a rodent model of breast cancer

Loic Van Horne², Jeff Saelens², Kennita Johnson², Sneha Rao², Paul Dayton^{1,2,3}, Ryan Gessner¹

1 – SonoVol, Inc. – Research Triangle Park, NC, 2 – UNC Chapel Hill/NC State University Joint Dept. of Biomedical Engineering 3 – Biomedical Research Imaging Center, UNC Chapel Hill

Abstract

Purpose:

In vivo bioluminescence imaging (BLI) plays an important role in the disease research and drug development pipeline. BLI has a limited depth of penetration and thus lack of anatomic information and context for where signals originate. Additionally, in situ morphological changes cannot be measured. With the addition of an anatomical modality, however, this paradigm shifts. Previous studies have shown BLI images co-registered with CT[1], and MRI[2] images of the same animal, though to our knowledge no in vivo studies have yet demonstrated alignment between high frequency 3D tomographic ultrasound (structural) and BLI (functional) images. Multimodality fusion yields many benefits, including more accurate region of interest definitions, more holistic understanding of anatomical context of in situ pathology, tomographic reconstruction of the BLI signal, and improvements in BLI spatial resolution. Contained herein is a proof of feasibility of a tomographic anatomical image acquisition with ultrasound (US) aligned with BLI images. Additionally, MR images were acquired of the same animals and compared to the 3D US data to confirm ROI accuracy.

Materials and Methods:

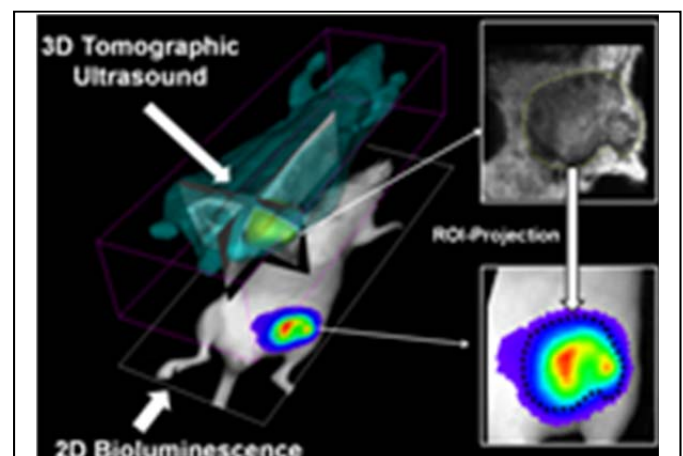
A xenograft model for breast cancer (MDA-MB-231) was generated in a small cohort of female nude mice (N=8). 1.5×10^6 cells were injected in a lower lateral inguinal mammary pad. US imaging was performed on a prototype whole body imaging device (SonoVol). Briefly, animals were positioned in the supine position and imaged at 30 MHz from several different angles (± 20 deg) over a field of view of $6 \times 3 \times 1.6$ cm. The position of the US transducer was precisely controlled via the system's robotic stage apparatus. The 2D US images were reconstructed into tomographic volumes offline. MRI images were acquired of each animal on the same day as the US images. Data taken with a T2 weighted protocol on a 9.4T system (Bruker), with isotropic scan resolution of 0.2 mm, and field of view of $4 \times 4 \times 4$ cm. Acquisition time was 1 hour. A standard 2D BLI protocol was acquired for all tumors on an IVIS Lumina. Four different readers defined ROIs within US and MRI datasets, from which 3D masks were generated. The volumes of the masks were then compared between the two modalities for each tumor. Images were aligned between 3D tomographic datasets and 2D BLI images via fiducial based registration.

Results:

3D tomographic US scans were acquired and reconstructed in < 10 min. None of the tumor volumes were statistically different between MRI and SonoVol datasets ($p > 0.05$ for all tumors). Average tumor diameter was 10.7 ± 7.0 mm. On average there was an inter-modality deviation (MRI vs. SonoVol) of 5.3% in reported volumes for the same tumors, and an average deviation between readers of 11.3%.

Conclusions:

Feasibility for whole-body tomographic anatomical imaging with US and registration with BLI has been established, with tumor ROI definition accuracy similar to MRI and a 6x decrease in image acquisition time.



(Left) A 3D composite image showing the alignment between the whole-body ultrasound anatomical image (top) and 2D BLI functional image (bottom). The two foci of BLI signal can be mapped directly to the tumor's two distinct

2 - Optimizing the Production of Hyperpolarized ^{129}Xe Gas for *in vivo* MRI Studies

Michael Antonacci^{1,2}, Alex Burant^{1,2}, Rosa T. Branca^{1,2}

¹*Department of Physics and Astronomy, University of North Carolina, Chapel Hill, NC 27599.*

²*University of North Carolina Biomedical Research Imaging Center, Chapel Hill, NC 27599.*

Abstract

Purpose:

Hyperpolarized ^{129}Xe (HPXe) gas is an excellent contrast agent, especially for the detection of lung ventilation function and brown adipose tissue. However, for its use in humans, high volumes at relatively high polarization levels are needed. Spin exchange optical pumping (SEOP) is the most widely used method to hyperpolarize ^{129}Xe gas, however, the conditions that lead to high polarization levels for large gas volumes are not well understood. The goal of this work is to understand better the physical processes and the experimental conditions that lead to low polarization yield during SEOP.

Materials and Methods:

Comsol Multiphysics, a finite element analysis software, was used to better understand fluid flow and heat transfer throughout the optical cell during the SEOP process under different experimental conditions, namely temperature, cell geometry, gas flow pressure, and gas composition. Low-field NMR spectroscopy, spectroscopic analysis of the polarizer pumping beam, and optically-detected electron paramagnetic resonance (OD-EPR) spectroscopy are used to monitor the nuclear spin polarization of ^{129}Xe and the electronic spin polarization of rubidium, respectively, throughout the optical cell.

Results:

Finite element analysis simulations show that uneven temperature conditions inside the optical cell during the hyperpolarization process lead to gas turbulence and most likely depolarization of ^{129}Xe gas through wall interactions. The optical beam also appears to be detuned from the D1 Rb resonance line, leading to loss of polarization efficiency.

Conclusions:

Preliminary results show that the standard experimental conditions used to produce large volumes of hyperpolarized ^{129}Xe gas are suboptimal and need to be optimized in order to improve polarization efficiency. Most likely, turbulences in the optical cells cause an increase in the number of Xe-wall interactions and ultimately ^{129}Xe depolarization. The detuning of the laser beam causes reduced photon efficiency. Future work includes monitoring of nuclear ^{129}Xe polarization as well as Rb electron spin polarization to understand how turbulence and laser detuning ultimately affect ^{129}Xe polarization.

Poster Presentation Author: Michael Antonacci

#4 - Resting State fMRI of the Ferret Brain: Sensory, Default Mode, and Higher-order Networks

Zhe C Zhou, Andrew P Salzwedel, Susanne Radtke-Schuller, Yuhui Li, Kristin K Sellers, Yen-Yu I Shih, Flavio Frohlich*, Wei Gao*

Translational research benefits from a diverse set of animal model species for the study of physiological and pathological brain networks. In particular, resting state functional connectivity has emerged as a powerful tool for the assessment of normal or aberrant large-scale brain connectivity. However, no such examination of functional connectivity has been performed in ferrets, an intermediate model species that has recently gained traction for the study of higher-order brain function. Here, we present evidence for distinct networks in the ferret brain that exhibit similar topology and connectivity patterns to those observed in humans. We performed independent component analysis (ICA) and graph theory analysis on resting state functional magnetic resonance imaging (fMRI) data collected from anesthetized female ferrets (*Mustela putorius furo*). A 10 minute resting state echo-planar imaging scan was performed for each animal using a Bruker 9.4T scanner. Animals were anesthetized with 0.5-1% isoflurane and xylazine and paralyzed with vecuronium bromide.

Group analysis from six animals reveal four distinct functionally connected sensory networks (visual, auditory, and two somatosensory/motor), and three inter-connected “higher-order” networks ($z > 1.96$). Among these higher-order networks, we identified a putative anterior default mode network (DMN) composed of the prelimbic, premotor, and dorsolateral and medial prefrontal frontal cortex (PFC). A putative posterior DMN was comprised of the cingulate, posterior parietal, higher-order visual, and higher-order somatosensory cortices. The last network was made up of the medial PFC and premotor cortex. Finally graph theory analysis revealed consistent cross-animal small-world network attributes ($p = 0.003$) of the ferret brain, indicative of economic and dynamic brain wiring. These results suggest the presence of distributed, functionally connected networks in the ferret brain similar to that of humans and monkeys (1). The similarity in the organization of these functional networks to those in the human brain further supports an expanded role of the ferret in basic and translational neuroscience. Gaps in the characterization of the ferret brain limit our ability to draw conclusive similarities between ferret and human brain networks; however, this study highlights the importance of further delineating subdivisions of the ferret brain using both structural and functional methods.

(1) Vincent JL, Patel GH, et al. Nature. 2007 May 3

* contributed equally

#5 - Optogenetic manipulation of VTA dopaminergic neurons and global patterns of functional neural connectivity

Heather K. Decot^{1,2}, Wei Gao^{3,4}, Joshua H. Jennings^{1,2}, Jenna A. McHenry², Pranish A. Kantak², Yu-Chieh Jill Kao^{4,5}, Manasmita Das^{4,5}, Ilana B. Witten⁷, Karl Deisseroth⁸, Yen-Yu Ian Shih^{1,4-6}, Garret D. Stuber^{1,2}

1. Curriculum in Neurobiology, 2. Departments of Psychiatry & Cell and Molecular Physiology, UNC Neuroscience Center, 3. Department of Radiology, 4. Biomedical Research Imaging Center, 5. Department of Neurology, 6. Department of Biomedical Engineering, 7. Department of Psychology, Princeton University, Princeton, NJ 8. Department of Bioengineering, Stanford University, Stanford, CA

Purpose: Proper signaling in neuromodulatory networks, such as the brain's dopaminergic system, is critical for normal brain function and is altered in disease states such as addiction. While understanding of the molecular, cellular and electrophysiological drug-induced changes following repeated drug exposure has advanced, much less is known about the circuit-level neuroadaptations that occur. Here, we will elucidate the role of dopaminergic dysregulation in aberrant brain function and how selective activity of the dopamine system affects large-scale brain network function.

Materials and Methods: To target DA neurons within the midbrain, tyrosine hydroxylase (TH)-Cre adult Long Evans rats were microinjected into the ventral tegmental area (VTA) with a Cre-inducible adeno-associated virus carrying the gene encoding channelrhodopsin-2 (ChR2), a light-gated cation channel fused to an enhanced yellow fluorescent protein (EYFP) (TH^{VTA}::ChR2 rats) or only EYFP (TH^{VTA}::control rats). Chronic optical fibers were stereotactically implanted bilaterally above the VTA to permit light delivery (5 ms pulse width, 473-nm wavelength, 10-mW light pulses) at 10, 20, 30, and 40 Hz to selectively activate DA neurons within this region. Two to five repeated trials were performed for each frequency. fMRI experiments were performed 5-6 weeks after surgery. Each rat was endotracheally intubated and ventilated with ~1.5% isoflurane and medical air. The ventilation rate and volume were adjusted to maintain end-tidal CO₂ (EtCO₂) within a range of 2.6-3.2% and oxygen saturation (SpO₂) above 96%. Rectal temperature was maintained at 37±0.5°C. Dexmedetomidine (0.1 mg/ml) and pancuronium bromide (1.0 mg/ml) were infused intraperitoneally for duration of scan. For CBV-weighted MRI, a tail-vein catheter was used to deliver monocrystalline iron oxide contrast agent at a dose of 30 mg Fe/kg. The D1 receptor antagonist, SCH23390 (0.6 mg/kg) was injected intravenously to explore its effects on CBV signal responses observed in TH^{VTA}::ChR2 rats. Single shot, single sampled GE-EPI sequences (BW= 300 kHz, TR= 1000 ms, TE= 8.107 ms, 80x80 matrix, FOV= 2.56 x 2.56 cm², slice thickness= 1 mm) were acquired using a Bruker 9.4T MR scanner and home-made surface coil. Automatic co-registration using SPM codes were applied to realign time-series data within subjects and then again across subjects. Data were then averaged across subjects in order to provide group-averaged fMRI maps using correlation coefficient (CC) method with reference to the optogenetic stimulation paradigm. Bonferroni correction was applied to adjust for the multiple comparisons of fMRI maps by dividing the significance level (p<0.05) by the number of brain voxels.

Results: To genetically target the expression of ChR2-EYFP into midbrain tyrosine-hydroxylase (TH)-positive DA neurons, we introduced a Cre-inducible adeno-associated virus encoded by ChR2 fused to an enhanced yellow fluorescent protein (ChR2-EYFP) into the VTA of TH-Cre adult rats. 5-6 weeks following surgery, we observed expression of ChR2-EYFP within the VTA and confirmed colocalization with TH via immunohistochemistry. Transient optogenetic activation of DA neurons within the midbrain caused significant regional CBV increases in downstream targets of the VTA including the dorsal and ventral striatum in TH^{VTA}::ChR2 rats, whereas TH^{VTA}::control rats displayed no significant CBV increases within these regions. One-way ANOVA followed by Bonferroni multiple-comparison tests revealed a frequency-dependent effect in TH^{VTA}::ChR2 rats with significantly lower CBV responses observed at 10 Hz in comparison to those found at 20, 30, and 40 Hz (p<0.05). We next investigated whether intravenous application of the DA D1 receptor antagonist SCH23390 would modulate the CBV responses displayed in the TH^{VTA}::ChR2 rats. Intravenous application of SCH23390 significantly attenuated the optical stimulation mediated CBV responses within these forebrain targets.

Conclusions: This study demonstrates significant CBV increases in the dorsal and ventral striatum following optogenetic activation of DA neurons within the VTA. These data suggest that aberrant DA neuromodulation may alter the neuronal activation patterns seen between these neurons and their postsynaptic target regions, providing mechanistic insight into how DA signaling alters global patterns of brain connectivity. Our future work will analyze existing resting-state fMRI datasets to identify network connectivity changes following optogenetic modulations.

#6 - Exercise diminishes obesity-associated Marrow Fat as quantified by Magnetic Resonance Imaging (MRI)

Maya Styner¹, Gabriel Pagnotti⁵, Xin Wu¹, Cody McGrath¹, Gunes Uzer¹, Buer Sen¹, Zhihui Xie¹, Mark Horowitz⁶, Clinton Rubin⁵, Xiaopeng Zong⁴, Martin Styner^{2,3}, Janet Rubin¹

University of North Carolina, Chapel Hill, NC, Departments of Medicine¹, Computer Science², Psychiatry³, and the Biomedical Research Imaging Center⁴; State University of New York, Stony Brook, NY, Department of Biomedical Engineering⁵; Yale University, New Haven, CT, Department of Orthopedics and Rehabilitation⁶

Abstract

Purpose:

The effect of marrow adipose tissue (MAT) on bone remains poorly understood. Using a μ CT measure of osmium to visualize and quantify MAT, we found that 6 weeks of high fat diet (HFD) increased MAT prior to attaining obesity. Here we asked whether MAT would respond to running exercise in the setting of diet-induced obesity (DIO).

Materials and Methods:

4-wk old female C57BL/6 mice were fed low fat diet (LFD) or HFD. After 12 wk, mice were divided into control (LFD, DIO) or exercise groups (LFD-E, DIO-E) with voluntary running wheels (n=7/group). Running distances were equivalent in LFD and DIO mice. Femoral MAT (osmium- μ CT) and μ CT tibial bone quantity were assessed. To increase reproducibility and prepare for future in-vivostudies, femoral MAT was also assessed via 9.4 Tesla MR resulting in fat and water intensity normalized image maps.

Results:

After 3 wks running, total body fat mass was double in DIO compared to DIO-E (p<0.05). Lean mass was also higher in DIO vs. LFD (p<0.01). Respiratory quotients were lower in DIO (p<0.01) suggesting use of fat energy. After 6 wks running, mice were significantly heavier in DIO vs LFD (p<0.001). Total femur MAT (osmium volume/femoral volume) was 6.2 ± 2.8 in LFD, 4.7 ± 2.1 in LFD-E, 9.0 ± 4.2 in DIO and 4.7 ± 2.9 in DIO-E (p<0.05 for an exercise). MAT quantified by MRI (fat signal/femoral volume) was 2.5 ± 1.1 in LFD, 1.2 ± 0.8 in LFD-E, 3.3 ± 1.5 in DIO and 0.5 ± 0.4 in DIO-E (p<0.001 for exercise, p<0.01 for DIO vs. DIO-E). Pearson correlation coefficient showed an appropriate correlation of MAT quantification between osmium- μ CT and MRI of 0.65 (95% CI 0.31-0.84, p-value=0.0012). Obese mice had similar relative amount of MAT to the controls, likely due to increased femoral volume in DIO (14% higher in DIO compared to LFD, p< 0.01). Trabecular BV/TV increased with exercise by 20% in both LFD and DIO groups, p<0.001. DIO did not affect BV/TV or cortical parameters. In conclusion, MAT normalized to femoral volume as assessed by either osmium- μ CT or MRI was significantly attenuated by exercise in obese mice as well as mice on LFD. Both measures are relativized to bone volume, which as DIO mice have increased femoral volume, shows MAT is increased in DIO.

Conclusions:

In summary, diet and exercise effect on bone quantity and marrow fat are maintained in the setting of obesity. In addition, we present a quantitative MRI image tool, which should allow longitudinal study of MAT during behavioral, pharmacologic and genetic modification.

Poster Presentation Author: Cody McGrath

#7 - Angelman Syndrome Mice Recapitulate the Altered Brain and White Matter Growth Observed in Angelman Syndrome Patients

M. Judson¹, A. Rumple², A. Burette¹, F. Budin², B. Philpot¹, and B. Paniagua²

1. Department of Cell Biology and Physiology. University of North Carolina at Chapel Hill.
2. Department of Psychiatry. Small Animal Image Processing Group. Neuro Image Research and Analysis Laboratories. University of North Carolina at Chapel Hill.

Abstract

Purpose:

White matter (WM) pathway deficits are common in neurodevelopmental disorders, including Angelman syndrome (AS). AS, caused by maternal allele deletions of UBE3A, is a debilitating disorder characterized by postnatal emergence of microcephaly, motor impairments, lack of speech, intellectual disability, and seizures. The few imaging studies performed to date suggest that AS individuals have generalized WM deficits, including loss of volume and possibly delayed myelination. However, as in other neurodevelopmental disorders, WM deficits in AS remain poorly defined, making it difficult to link them to behavioral phenotypes and, consequently, to establish their value as therapeutic biomarkers.

We want to elucidate the anatomical and pathophysiological basis for WM deficits in AS, using an AS model mouse (*Ube3a^{m-/p+}*). We want to demonstrate that the animal model exhibits generalized WM pathway impairments that mirror those found in AS individuals, both at the macroscopic and microscopic levels, using magnetic resonance imaging (MRI) diffusion tensor imaging (DTI) and ultrastructural electron microscopy (EM).

Materials and Methods:

13 C57BL/6J mice (6 *Ube3a^{m-/p+}* and 7 *Ube3a^{m+/p+}* littermate controls) were scanned in 2012 and 2013. They were aged PND70-PND90.

The data was processed using an in-house pipeline consisting of unbiased, atlas based, regional segmentation. Atlas segmentation based on 20 regions from the C57 Brookhaven atlas Region-based statistics were calculated for each subject and included volumes, means, and standard deviations of the intensity in the segmented regions or over the whole mask.

Processing and group analysis of DTI data are based on procedures that provide consistent parameterization between subjects. These procedures yield a final average tensor atlas for tractography of targeted tracts, which will form the basis of data extraction and analysis from individual data sets.

Results:

Significant changes were found in the volumes of several regions of interest. Volumes for AS mice were reduced in the corpus callosum ($p=0.0006$), the internal capsule, the anterior commissure, the fornix, and the fimbria. FA in AS mice was significantly lower in the internal capsule.

Conclusions:

AS mice exhibit developmental reductions in brain weight, despite increases in body weight, indicating they have microcephaly with postnatal onset. Microcephaly similarly emerges during postnatal development in individuals with AS. Reduced callosal volume in AS mice also arises postnatally, and significantly exceeds corresponding reductions in neocortical grey matter, indicating that WM pathology is a major contributor to the microcephaly. Our preliminary EM data from adult AS mice indicate that callosal volumetric reductions result from reductions in axon caliber rather than deficient myelination. Importantly, our preliminary DTI data show evidence of reduced WM integrity in adult AS mice, supporting that altered WM trajectories in AS culminate in abnormal WM structure in key motor pathways.

Poster Presentation Author: _____ Yes _____

#8 - Corpus Callosum and Cerebellum Shape Changes After Prenatal Ethanol Exposure

A. Rumble¹, S.E. Parnell^{1,2}, F. Budin¹, and B. Paniagua¹

1. *Department of Psychiatry. Small Animal Image Processing Group. Neuro Image Research and Analysis Laboratories.* 2. *Department of Cell Biology and Physiology. Bowles Center for Alcohol Studies. University of North Carolina at Chapel Hill.*

Abstract

Purpose:

Prenatal ethanol exposure is one of the leading causes of birth defects, yet the full spectrum of ethanol's effects are still not understood. One reason for this lack of understanding is that ethanol has significantly different actions depending on the period of prenatal exposure. For example, exposure during gastrulation induces deficits along the holoprosencephaly spectrum, however, exposure at slightly later stages (neurulation), does not. Ethanol exposure during neurulation in mice has been shown to induce behavioral anomalies involving disinhibition, sociability and motor function. This current study was designed to examine potential brain abnormalities underlying these behaviors.

To identify and precisely document ethanol-induced shape changes in localized brain regions and specifically to quantify the location of the the volume differences of cerebellum and corpus callosum in individuals exposed prenatally to ethanol.

Materials and Methods:

19 C57BL/6J mice, 10 ethanol exposed on gestational day 8 and 9 controls, were sacrificed and perfused at postnatal day 45. 6 direction DTI images with a b-Value of 1595 were acquired on the 9.4T magnet at Duke University. The scan time was 12.75 hours. The field of view was 22mm x 11mm x 11mm. The TR was 100ms; TE was 11.82ms. The data was processed using an in-house pipeline consisting of unbiased, atlas based, regional segmentation.

Atlas segmentation based on 20 regions from the C57 Brookhaven atlas Each subject's final segmentation was visually checked by our anatomical expert for quality control. Region-based statistics were calculated for each subject and included volumes, means, and standard deviations of the intensity in the segmented regions or over the whole mask. Regions of interest (ROIs) used for this study include cerebellum and corpus callosum.

Spherical HARMonic representation Point Distributed Models (SPHARM-PDM), was used. Corpus and Cerebellum ROIs were used as inputs to generate first a spherical harmonic representation of 3D shape and then a correspondent triangulated surface. After a quality check to ensure data integrity and correspondence establishment, individual PDMs of regions were grouped by treatment condition. 3D models were separated in different treatment groups and compared using a permutation testing based multivariate analysis of covariance.

The outputs of these analyses include heat maps indicating areas of statistically significant shape differences and color coded projections of those differences between the mean 3D shape of control and ethanol-exposed subjects groups.

Results:

Towards the splenium of the corpus callosum, the control animals were significantly bigger than the ethanol treated animals. Along the ventral surface of the corpus callosum, however, the ethanol treated animals were significantly bigger. On the anterior dorsal face of the cerebellum the control animals were significantly bigger than the ethanol treated animals. Along the underside, the ethanol treated animals were significantly bigger than the controls.

Conclusions:

This work demonstrates areas of the brain that may be related to behavioral abnormalities following an acute prenatal ethanol exposure and should be explored further

#9 - Evaluation of the Accuracy of Computed Tomography and Micro-Computed Tomography of the Feline Carpus

Erin M. Koballa¹, Caroline E. Webster², Denis J. Marcellin-Little^{1,2}, Susan Bernacki³, Ola L.A. Harrysson², & Ian Robertson⁴

¹Dept. of Clinical Sciences, College of Veterinary Medicine (CVM), North Carolina State University, Raleigh, NC (NCSU); ²Fitts Dept. of Industrial and Systems Engineering, College of Engineering (CoE), NCSU; ³Dept. of Biomedical Engineering, CoE, NCSU; ⁴Dept. of Molecular & Biomedical Sciences, CVM, NCSU

Abstract

Purpose:

Computed tomography (CT) scanning is the established method used to capture bone anatomy when planning complex orthopedic procedures such as custom total joint arthroplasty and hemiarthroplasty. The potential lack of resolution of CT scans decreases the accuracy of reconstructed CT image data and could negatively impact surgical planning and implant design. This lack of accuracy may increase the risk of complications for the patient because of suboptimal implant fit or accelerated wear. The aim of the current project includes assessing accuracy of CT compared to high resolution methods: micro-computed tomography (μ CT) and laser-based coordinate measuring machine (CMM).

Materials and Methods:

Sixty-one forelimbs were harvested from cats euthanized for reasons independent from this study. Samples were kept frozen at -20C and tissue preserved with sterile gauze saturated with saline. Twenty-three specimens were eliminated because they were skeletally immature and deemed unusable for this study. Due to costs and feasibility, a sample size of twenty was selected. Each specimen was scanned using four imaging methods: CT (clinical and perpendicular positioning), μ CT, and CMM. Three-dimensional computer assisted design models generated from all four scans were aligned so that all images were superimposed over one another using Materialise and Geomagic Qualify computer assisted design software. Dorsopalmar (DP) and mediolateral (ML) radius of curvature, DP and ML length, and surface deviation were measured and compared statistically using CMM as the gold standard.

Results:

For surface deviation, μ CT differed the least from the CMM with an average positive deviation of 0.03 mm and an average negative deviation of 0.02 mm. Clinical positioning CT differed with an average positive deviation and average negative deviation of 0.14 and 0.24, respectively. Perpendicular positioning CT differed with the CMM by an average positive deviation of 0.20 mm and 0.28 mm. For ML length, there was no statistically significant difference ($p>0.05$) between clinical and perpendicular positioning for CT. There was a statistical significant of $p<0.05$ for all other comparisons of imaging modalities. For DP length, there was no significant difference between the CMM and μ CT ($p>0.05$), and there was statistical significance between all other comparisons ($p<0.05$).

Conclusions:

With the poor quality of the clinical CTs, it is likely that current resolutions of clinical CT imaging are not suitable for custom patient specific implant and prosthetic design in small joints. This study focuses on the distal radial carpal joint; however, broader reaching implications include joints in other species that are similarly sized or small including but not limited to human interphalangeal joints and the human temporomandibular joint.

#10 - Developing Thiol-Reactive Vinyl Sulfone for Site Specific ^{18}F -Labeling of Peptides and Proteins

Ben Giglio, Zhanhong Wu, Zibo Li
Biomedical Research Imaging Center, Department of Radiology

Abstract (less than 500 words)

Purpose:

Accumulating evidence suggests that neurotensin receptors (NTRs) play key roles in cancer growth and survival. In this study, we developed a simple and efficient method to radiolabel neurotensin peptide with ^{18}F for NTR-targeted imaging.

Materials and Methods:

The thiol-reactive reagent ^{18}F -(2-(2-(2-fluoroethoxy)ethoxy)ethylsulfonyl)ethane (^{18}F -DEG-VS) was facilely prepared through 1-step radiofluorination. After high-pressure liquid chromatography purification, ^{18}F -DEG-VS was incubated with the c(RGDyC) and c(RGDyK) peptide mixture to evaluate its specificity toward the reactive thiol. Thiolated neurotensin peptide was then labeled with ^{18}F using this novel synthon, and the resulting imaging probe was subjected to receptor-binding assay and small-animal PET studies in a murine xenograft model.

Results:

^{18}F -DEG-VS was obtained in high labeling yield. The reaction of ^{18}F -DEG-VS was highly specific for thiols at neutral pH, whereas the lysine of c(RGDyK) reacted at a pH greater than 8.5. ^{18}F -DEG-VS-c(RGDyC) was the preferred product when both c(RGDyK) and c(RGDyC) were incubated together with ^{18}F -DEG-VS. Thiolated neurotensin peptide (Cys-NT) efficiently reacted with ^{18}F -DEG-VS, with a 95% labeling yield (decay-corrected). The radiochemical purity of the ^{18}F -DEG-VS-NT was greater than 98%, and the specific activity was about 19.2 ± 4.3 TBq/mmol. Noninvasive small-animal PET demonstrated that ^{18}F -DEG-VS-NT had an NTR-specific tumor uptake in subcutaneous HT-29 xenografts. The tumor-to-muscle, tumor-to-liver, and tumor-to-kidney ratios reached 30.65 ± 22.31 , 11.86 ± 1.98 , and 1.91 ± 0.43 at 2 h after injection, respectively, based on the biodistribution study. Receptor specificity was demonstrated by blocking experiment.

Conclusions:

We have established a facile ^{18}F -labeling method for site-specific labeling of the Cys-NT. Using this method, we synthesized an NTR-targeted PET agent, which demonstrated high tumor-to-background contrast.

Poster Presentation Author: _____ *Ben Giglio*_____